

# Joint Characteristics of Cu-Ni Alloy Fabricated by GTAW and MPAW Processes: A Comparative Study

DOI : 10.22486/iwj.v57i1.223725

ORCID: Swagat Dwibedi: <https://orcid.org/0000-0002-3124-9920>  
ORCID: Swarup Bag: <https://orcid.org/0000-0003-2553-831X>

**Swagat Dwibedi and Swarup Bag\***  
Department of Mechanical Engineering  
Indian Institute of Technology Guwahati  
Guwahati 781039, Assam, India  
email: swagatsudhadwibedi@iitg.ac.in  
\*Corresponding author email: swarupbag@iitg.ac.in



## Abstract

The current work presents a comparative analysis of the joint behavior of Cu-Ni alloy weldments fabricated by Micro-Plasma Arc Welding (MPAW) and Gas Tungsten Arc Welding (GTAW) processes. The Cu-Ni alloy thin sheets are fabricated at different values of heat input ( $\sim 40$ - $135$  J/mm) by MPAW and GTAW processes, respectively. Further, to evaluate their characteristics, joints are subjected to metallurgical, mechanical, and electrochemical testing. The joints fabricated with a higher magnitude of heat input resulted in deteriorated surface quality with a value of  $R_a \sim 6.13$   $\mu\text{m}$ . The increased surface roughness value of the joints resulted in a higher corrosion rate (1.273 mm/year). A finer microstructural morphology is achieved for lower heat input condition. Accordingly, the weldment exhibited higher joint efficiency of  $\sim 91\%$ . The prominent reason for achieving higher joint strength is related to the presence of lower secondary dendritic arm spacing (SDAS), which enhances the joint strength and ductility for the joints as compared to higher SDAS value. Further, the micro-fractography analysis reveals the presence of micro/macro-voids for high heat input, whereas the existence of numerous dimples of varying size and depth is observed for low heat input condition, implying the role of heat input of utmost importance.

**Keywords:** Heat input, Surface Quality, Joint strength, Fracture analysis, Corrosion behavior

## 1.0 INTRODUCTION

Heat input and power density play a significant role in determining the quality of the weld joint. With the increase in power density of the heat source, the amount of heat input required to produce weld joints decreases. Reduction in the amount of heat input leads to increased penetration, weld speed, and most importantly, a lesser extent of damage to the component to be welded [1]. The significance of optimum heat input amplifies as the thickness of the material reduces because thin structures are more susceptible to melt-through, extensive heat-affected zone, weld-induced deflection, and loss of vital alloying elements [2]. The selected welding

process decides the power density, and the selected process parameters govern the heat input utilized to form the joint. The power density in decreasing order can be mentioned a high-energy beam density process followed by arc-based joining techniques [3,4]. Arc-based joining techniques may be preferred where joint tolerance is a significant concern. Also, cost-effectiveness allows arc-based joining techniques to surpass the high-power density processes [5]. The joining of thin sheets is generally accomplished by autogenous mode, wherein filler material is not required. Hence, non-consumable arc-based welding processes are the only viable option available, i.e., Gas tungsten arc welding (GTAW) and micro-plasma arc welding (MPAW) can be opted for the successful

joining of thin sheets. MPAW is derived from the GTAW process, wherein the positioning of the electrode inside the nozzle results in the constriction of the arc, thus increasing the power density [6-8]. In recent times, GTAW and MPAW have been used to join thin ( $\leq 1.5$  mm) sheets with a wide variety of materials. SS304L [9], IN625 [10], IN718 [11], Ti-5Al-2.5Sn alloy [12], GH4169 superalloy [13], and HSLA S500MC [14] have been successfully joined using the GTAW process. Ti-6Al-4V [15,16], Maraging steel [17], SS316L [18,19], SS316L-IN718 [20], IN718 [21], AMg6 alloy [22] have been welded with sound joint quality by employing MPAW process. It may be noticed that the joining of thin Cu-Ni alloy is yet to be explored in a comparative manner involving GTAW and MPAW processes.

The joining of Cu-Ni alloy has been explored by a few researchers recently [23-29]. 90-10 Cu-Ni and 70-30 Cu-Ni alloys of Cu-Ni were joined using the laser beam welding (LBW) technique to understand the behavior of process conditions on the bead geometry and metallurgical variation in the joints. The authors reported complete penetration at 6 kW, 0.02667 m/s process conditions, and a decrease in the SDAS value was reported with an increase in laser energy [23]. 90-10 Cu-Ni flux-cored arc welding (FCAW) was accomplished using 70-30 Cu-Ni as filler material, and the joints were evaluated to examine metallurgical and mechanical behavior. Generated weld defects (porosity and spatter) were reported over the acceptable range, and the fractured surface revealed dimple features in the failed region [24]. GTAW process was utilized to perform repeated joining (repair) of 70-30 Cu-Ni alloy for naval purposes. The authors reported enhancement in the heat-affected zone (HAZ) and a 27 % reduction in impact strength due to repeated welding repair [25]. A CO<sub>2</sub> LBW was used to join 70-30 Cu-Ni alloy using 3.5 kW and 1.0-2.5 m/min. The produced joints were further analyzed to study microstructure-mechanical property relations. The authors reported the presence of uniformly spaced equiaxed fine grains in the fusion zone at 1.5 m/min weld speed, which resulted in enhanced joint quality [26]. A 5.2 kW Yb-Fiber LBW was utilized to join 70-30 Cu-Ni alloy, and the joint characteristics were verified as per ISO standards. 5.2 kW and 1.5 mm/min were reported as optimized parameters with existing undercuts and porosities formed in the fusion zone (FZ) within specified standards [27]. MPAW was conducted on 90-10 Cu-Ni alloy at different heat inputs, 40.44, and 104.76 J/mm, and a comparison was reported based on destructive and non-destructive examination. The authors reported a reduction in joint strength from  $\sim 292$  to  $\sim 227$  MPa and an increase in the total pores (voids) from 32 to 90 as the heat input increased from 40.44 to 104.76 J/mm [28]. The GTAW process was used to join 90-10 Cu-Ni alloy, and the corrosion behavior of the joints was studied in a detailed manner. As a result of the comparatively lower density of adhesion, the highest corrosion

rate is reported in the HAZ [29]. The literature on Cu-Ni alloy lists down the primary concerns in the joining of Cu-Ni alloys as (i) the occurrence of solidification cracks in the FZ, (ii) the development of liquation cracks tendency in the region adjacent to fusion boundary (FB), i.e., HAZ, (iii) the possibility of cracks (ductility-dip) during repair welding process, and (iv) pore formation in the FZ [27]. To avoid the occurrence of such defects in the joining of Cu-Ni alloy, demands careful selection of process parameters. For non-consumable arc-based joining techniques, heat input is considered as the primary input parameter that is held responsible for the quality of joints produced [30].

The in-depth above-discussed review of Cu-Ni alloy is summarized in a point-wise manner in **Table 1**. It may be noted that Cu-Ni alloy joints have been separately analyzed using MPAW and GTAW processes, but a comparison in joint characteristics for thin Cu-Ni alloy joints is yet to be reported. Also, the influence of heat input on the metallurgical, mechanical, and electrochemical behavior of Cu-Ni alloy is yet to be explored in a detailed fashion. Hence, in the current experimental methodology, an attempt is made to join a thin sheet of Cu-Ni alloy using different arc-based joining techniques with minimum heat input conditions available for the respective processes. Further, the joint characteristics are analyzed comparatively to reveal the importance of process and process parameters to achieve the successful joining of thin sheets.

## 2.0 MATERIALS AND METHODS

In the present experimental study, a thin sheet of Cu-Ni (90-10) alloy is selected for autogenous joining by MPAW and GTAW processes. The process conditions used for the joining are represented in **Table 2**. The primary input for a joining process is heat input, and other parameters may be treated as secondary, which do not influence much of the joint characteristics. The integration of weld current with weld speed is treated as heat input, given as Eq. (1).

$$\text{Heat input (J/mm)} = \frac{\text{current(A)} \times \text{voltage(V)}}{\text{speed (mm/s)}} \times \eta \quad \dots(1)$$

wherein the value of  $\eta$  (efficiency) is considered 0.66 for the MPAW process [28] and 0.60 for the GTAW [31] process. Utilizing the data from **Table 2**, the heat input is evaluated as 40 J/mm for MPAW and 135 J/mm for the GTAW process. Accordingly, the nomenclature is provided as MPAW $\rightarrow$ S<sub>40</sub> and GTAW $\rightarrow$ S<sub>135</sub>. The selected weld conditions are subjected to different characterization techniques, and a comparative analysis is presented between them (S<sub>40</sub> and S<sub>135</sub>).

Table 1 : Summarizes past work on joining of Cu-Ni alloy

[Ref.]	Authors	Material(s)	Process	Key findings
[23]	Ferro et al.	90-10 Cu-Ni, 70-30 Cu-Ni	LBW	A higher value of laser power resulted in increased SDAS value. Due to higher power density, no grain coarsening was reported in the HAZ.
[24]	Devletian et al.	90-10 Cu-Ni	FCAW	Due to the presence of porosity, the tensile specimens failed from the FZ with dimple features in the failed regions.
[25]	Munro	70-30 Cu-Ni	GTAW	Repeated joining resulted in an enhancement in the HAZ and a 27 % reduction in impact strength.
[26]	Chakravarthy et al.	70-30 Cu-Ni	LBW	At 1.5m/min weld speed, the FZ revealed Al uniformly spaced equiaxed fine grains that resulted in enhanced joint quality.
[27]	Cao and Nolting	70-30 Cu-Ni	LBW	Undercut and porosities formed in the weld joint were within specified standards.
[28]	Dwibedi and Bag	90-10 Cu-Ni	MPAW	Higher heat input yielded a greater number of pores and pore size.
[29]	Xing et al.	90-10 Cu-Ni	GTAW	As a result of the comparatively lower density of adhesion, the highest corrosion rate is reported in the HAZ.

Table 2 : Process parameters used to fabricate Cu-Ni alloy

Process parameters	GTAW	MPAW
Welding current (A)	30	15
Welding speed (mm/s)	1.07	6.12
Plasma gas flow rate (lpm)	-	0.7
Shielding gas flow rate (lpm)	10.2	5.5
Electrode diameter (mm)	1.6	1.0
Nozzle diameter (mm)	2.4	1.2
SOD (mm)	2	
Polarity → DCEN, Welding mode → Continuous		

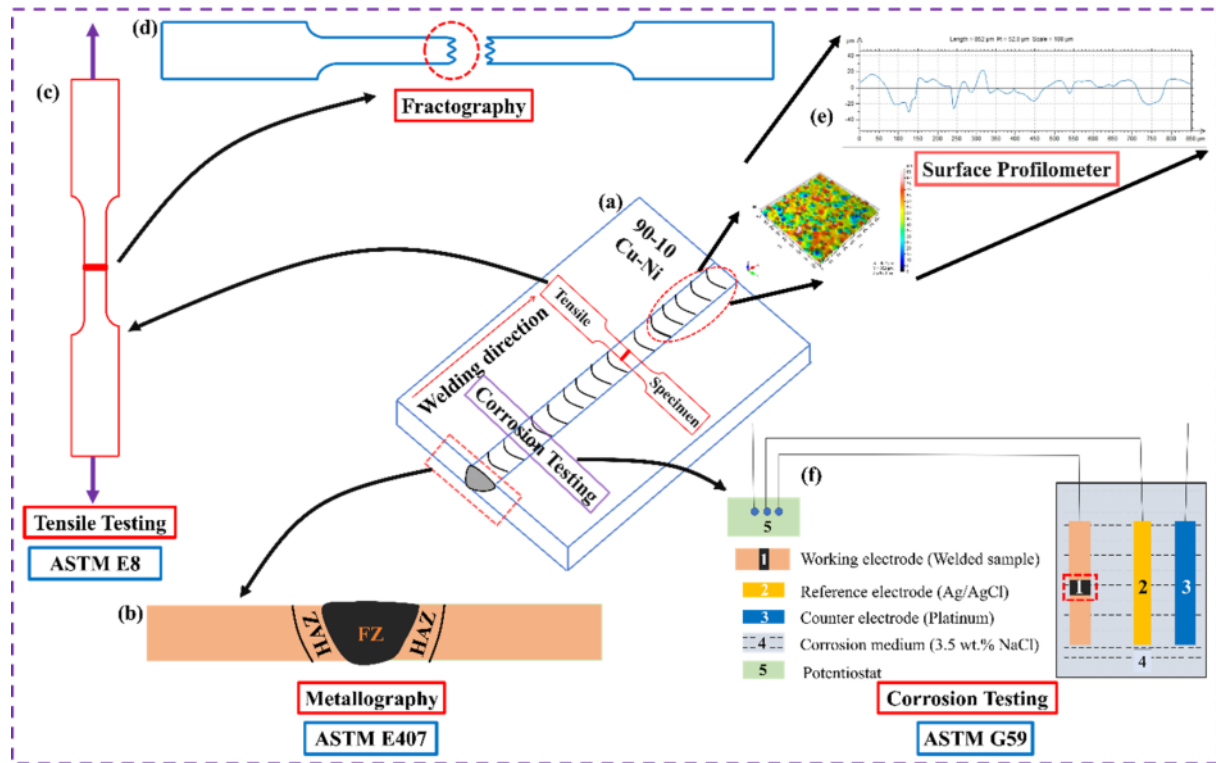


Fig 1 : Represents (a) weld specimen, (b-f) metallography analysis, tensile test, fracture analysis, surface roughness, and corrosion test coupons with the corresponding ASTM standards

**Fig. 1(a-e)** depicts the methodology used for the current experimentation. **Fig. 1(a)** represents the weld specimen from which standard coupons are extracted to study the microstructural, mechanical, and electrochemical behavior of the welded specimen as per ASTM standards. **Fig. 1(b)** depicts the sample considered for metallography analysis to reveal the different regions (fusion zone → FZ and heat-affected zone → HAZ) of the specimen. **Fig. 1(c)** shows the standard tensile coupon carried out at 0.5 mm/min to quantify the joint strength. Further, the failed tensile coupons are investigated to identify the mode of failure of the joints, shown in **Fig. 1(d)**. The surface quality of the joints provides vital information regarding the overall acceptability of a joint. The absence of any visual imperfections is a criterion for the initial screening of the joints, but quantifying the value needs to be done by measuring the surface roughness value, as shown in **Fig. 1(e)**. Along with metallurgical and mechanical properties, the electrochemical behavior of the joints is also conducted to measure the corrosion behavior of the joints under a selected corrosion media, as predicted in **Fig. 1(f)**.

### 3.0 RESULTS AND DISCUSSION

#### 3.1 Bead Profile and Surface Quality

The macroscopic images (top surface) of the welded specimen are illustrated in **Fig. 2(a,b)**. A continuous weld bead without any visible flaws is observed for both cases  $S_{40}$  and  $S_{135}$ . Weld bead with different zones FZ and HAZ is clearly demarcated with fusion boundary (FB). The visual inspection of a weld joint is considered to be the first inspection, followed by destructive and non-destructive analysis. The macroscopic images suggest the absence of any visual defect such as undercut, spatter, and lack of fusion. Two notable changes observed from the images reveal (i) a change in the bead size (FZ and HAZ) and (ii) a change in the bead color. With the rise in heat input value, the bead size (FZ) increases from  $\sim 1.31$  ( $S_{40}$ ) to  $\sim 2.49$  mm ( $S_{135}$ ). Due to the rise in the heat input, the heat flux affects the wider area of the base metal (BM), resulting in more melting, and thus, the bead size increases [8]. As the heat input increases from 40 J/mm ( $S_{40}$ ) to  $S_{135}$  J/mm ( $S_{135}$ ), another major change to be noted is the change in the appearance of the bead profile from dark brown ( $S_{40}$ ) to black color ( $S_{135}$ ). The probable reason for the transition of the color of the weld bead

is due to higher chances of contamination taking place at higher input value (135 J/mm  $\rightarrow$   $S_{135}$ ). A smooth surface is a mandatory requirement for a weld to qualify as a sound joint, along with complete penetration through the thickness [32]. To further analyze the surface properties, the quality of the joints is evaluated using a surface profilometer (Make: Taylor Hobson). From the center of the FZ, a section of  $\sim 850 \mu\text{m}^2$  is scanned, and its topological picture in 3D for the cases  $S_{40}$  and  $S_{135}$  is illustrated in **Fig. 2(c,d)**. The comparative variation in the unevenness of the FZ and a significant change in the topology can be observed. Such changes result due to severe agitation caused as a consequence of prolonged exposure to the thermal cycle for case  $S_{135}$ . Whereas, for the  $S_{40}$  weld condition, limited exposure to a comparatively lower heat input (40 J/mm) corresponds to a smooth weld surface. Further,

surface roughness is measured along the longitudinal section of the FZ. For the  $S_{40}$  weld condition, a minimum variation in the surface topography is observed, whereas for the  $S_{135}$  weld condition, unevenness is observed throughout the area of scan. **Fig. 2(e,f)** shows the variation in the value of surface roughness ( $R_a$ ) along a selected line in the obtained 3D topological figure. **Table 3** represents the weld bead characteristics for  $S_{40}$  and  $S_{135}$  weld joints. The experimentally determined value of surface roughness ( $R_a$ ) increases from  $0.438 \mu\text{m}$  to  $6.13 \mu\text{m}$  with an increase in heat input from 40 J/mm ( $S_{40}$ ) to 135 J/mm ( $S_{135}$ ). An increase in the  $R_a$  value can lead to an easy path for initiating a crack [33] and also provide an easy site for attack when exposed to a corrosive environment [34]. The influence of the value of  $R_a$  on the electrochemical behavior of the Cu-Ni alloy is discussed in-depth in the corrosion analysis section.

Table 3 : Represents the weld bead characteristic

Weld condition	Bead size (mm)	Bead color	Surface Roughness ( $\mu\text{m}$ )
$S_{40}$	1.31	Dark brown	0.438
$S_{135}$	2.49	Black	6.13

### 3.2 Metallurgical Analysis

To study the mechanical properties of a welded joint, it becomes mandatory to understand the microstructural changes that a material undergoes after completion of solidification. The metallurgical analysis is completed by analyzing and comparing the images obtained from optical and electron microscopes. **Fig. 3(a-f)** illustrates the microstructural morphology of different weld conditions, **Fig. 3(a-c)**  $\rightarrow$   $S_{40}$  and **Fig. 3(d-f)**  $\rightarrow$   $S_{135}$ . The white line near the weld interface demarcates the FZ and BM. Inside the FZ, yellow lines separate the areas where the formation of different structures is observed. The type of structure formed G/R and G $\times$ R govern the resulting microstructure, wherein G  $\rightarrow$  temperature gradient, and R  $\rightarrow$  rate of solidification. The solidification mode is controlled by the G/R ratio, i.e., a low value of the G/R ratio corresponds to equiaxed dendritic morphology, whereas a high value of the G/R ratio corresponds to columnar/cellular dendritic structure. The G and R product represents the cooling rate, which governs the size of the resulting microstructural morphology in the FZ [35]. Near the FB due to higher G, columnar structure is observed, whereas, in the center of the FZ, an equiaxed structure is noticed. **Fig. 3(b,c)** and **Fig. 3(e,f)** show the area near the FB at higher magnification to reveal the columnar structure formed

near the FB. To further examine the growth of the dendritic structure, an electron microscope is focused on the separate regions of FZ, where equiaxed and columnar structures were spotted. **Fig. 4(a)** characterizes the equiaxed microstructural structure established at the weld center. **Fig. 4(c-e)** shows different dendritic features, i.e., primary, secondary dendritic arm and spacing between them (PDAS, SDAS). PDAS is marked with yellow and SDAS is shown in red color. The SDAS depends on the value of G $\times$ R (cooling rate), which depends on the amount of heat input. For an increase in the value of heat input 40  $\rightarrow$  135 J/mm, the G $\times$ R value decreases, increasing the SDAS. As more time is available for solidification, the PDAS/SDAS grows. The incomplete growth of PDAS/SDAS changes to complete and the same is reflected in **Fig. 4(b)** (incomplete growth)  $\rightarrow$  **Fig. 4(c)** (partial growth)  $\rightarrow$  **Fig. 4(d)** (complete growth). In **Fig. 4(b)**, PDAS of larger width and limited growth of SDAS is observed, which changes to underdeveloped PDAS and considerable growth of SDAS. **Fig. 4(c)** represents the complete growth of PDAS and SDAS. The relation between SDAS and cooling rate is given by Eq. (2) [23], where it can be quantified that the value of SDAS increases from  $S_{40}$  to  $S_{135}$ .

$$\text{SDAS} = 33.683 (\text{Cooling Rate})^{-0.2512}$$

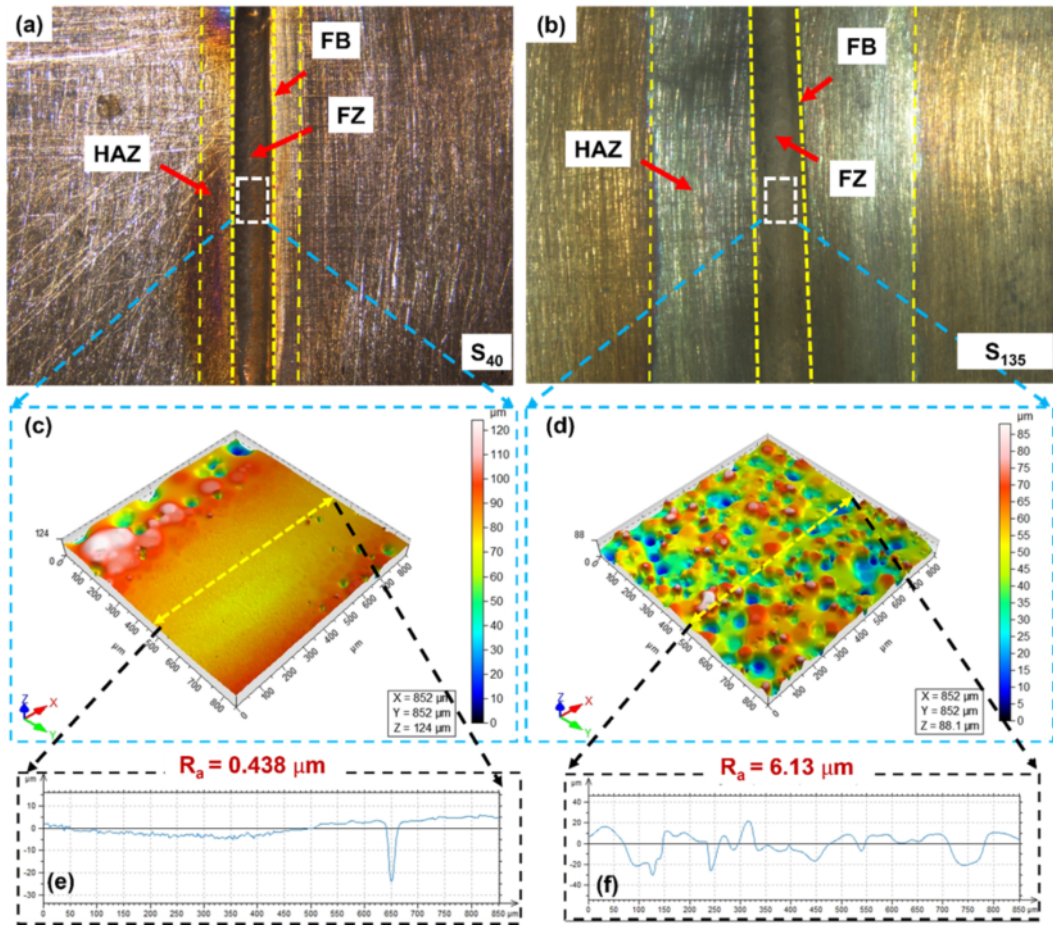


Fig. 2 : Depicts the top view of the welded specimen and surface condition for different weld conditions (a,c,e) S<sub>40</sub> and (b,d,f) S<sub>135</sub>

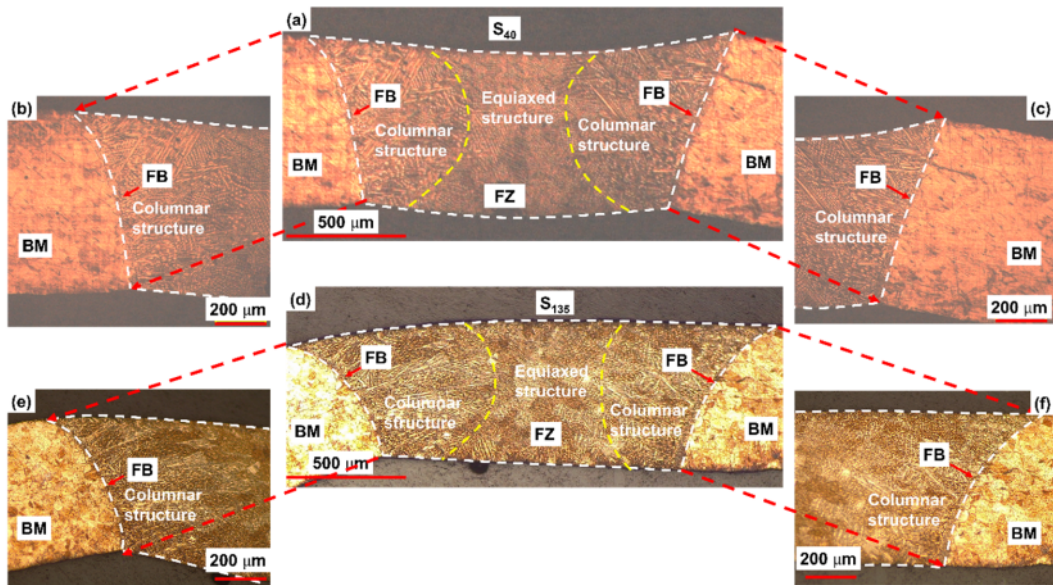


Fig. 3 : Illustrates microstructural morphology for different weld conditions (a-c) S<sub>40</sub> and (d-f) S<sub>135</sub>

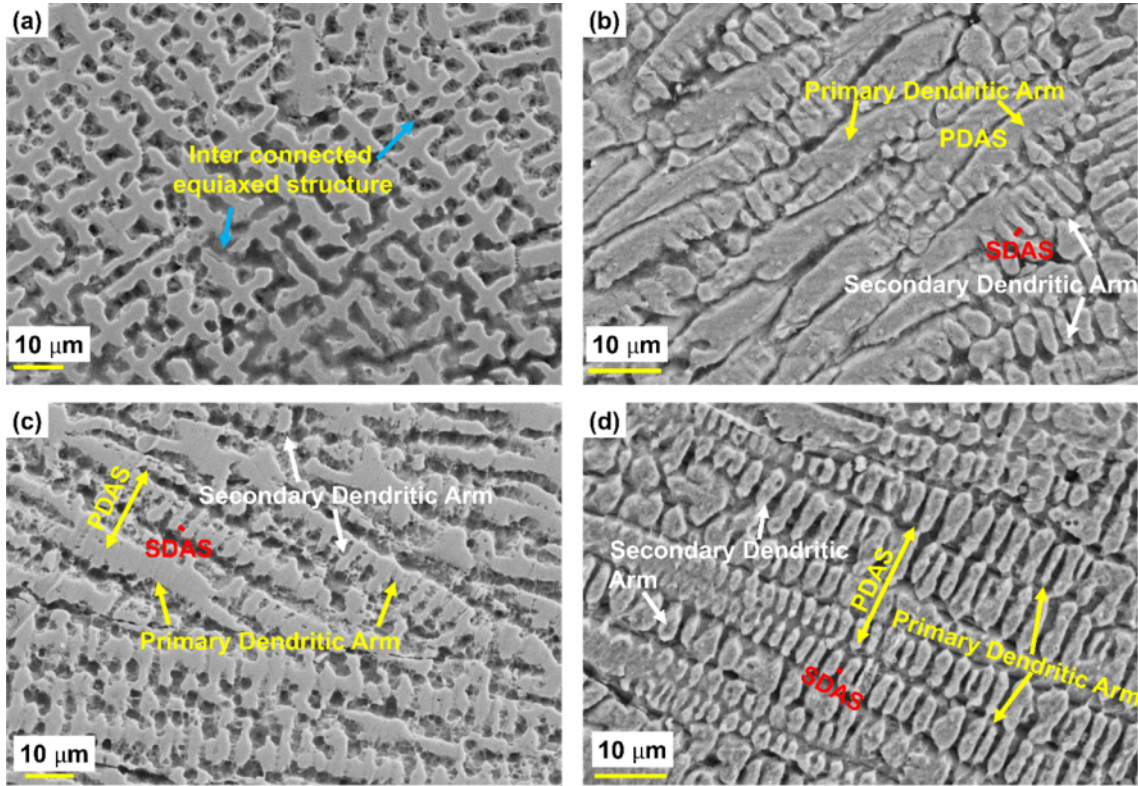


Fig 4: (a-d) Illustrates different microstructural morphology, PDAS, and SDAS obtained in the FZ

### 3.3 Joint Strength and Failure Analysis

The mechanical test is carried out to quantify the joint strength of the welded specimens. Standard specimens are prepared, and a tensile test is performed at a uniform strain rate (0.5 mm/min). The engineering stress-strain curve is plotted, and significant features are extracted from the graph. **Fig. 5(a)** illustrates the engineering stress-strain curve, and **Fig. 5(b)** shows the evaluated joint efficiency and obtained ductility for different weld conditions ( $S_{40}$  and  $S_{135}$ ). The achieved result shows a significant decrease in the value of joint strength ( $\sim 292$  MPa for  $S_{40}$   $\rightarrow$   $\sim 203$  MPa for  $S_{135}$ ) as well ductility (39 %  $\rightarrow$  14 %) with an increase in the value of heat input from 40 J/mm ( $S_{40}$ ) to 135 J/mm ( $S_{135}$ ). The corresponding value of joint efficiency is evaluated as  $\sim 91$  % for  $S_{40}$  and  $\sim 63$  % for  $S_{135}$ . A drastic decrease in the joint strength ( $\sim 89$  MPa) and ductility (25 %) is noted and the probable reasons are listed as (i) an increase in the  $R_a$  (0.438  $\rightarrow$  6.13  $\mu\text{m}$ ) value can lead to an easy

path for the initiation of a crack [33], (ii) lower heat input (40 J/mm) leads to decreased SDAS value, and refined metallurgical morphology, which ultimately enhances the strength and ductility [27]. The quantitative data obtained from the tensile test is represented in **Table 4**. The failed tensile specimens are further analyzed to understand the behavior of failure further. **Fig. 6(a,b)** represents the fracture surface of the failed tensile specimens for different weld conditions  $S_{40}$  and  $S_{135}$ . The failed specimen reveals the presence of micro-and-macro voids for the  $S_{135}$  condition, whereas the existence of numerous dimples of varying size and depth is observed for the  $S_{40}$  weld condition. Thus, the failure mode varies from desirable ductile mode (characterized by numerous dimples for  $S_{40}$ ) to unwanted brittle mode (identified by the presence of micro-and macro-voids for  $S_{135}$ ) as the heat input increases. Another reason for inferior joint properties is the change in the failure mode (ductile mode  $\rightarrow$  brittle mode).

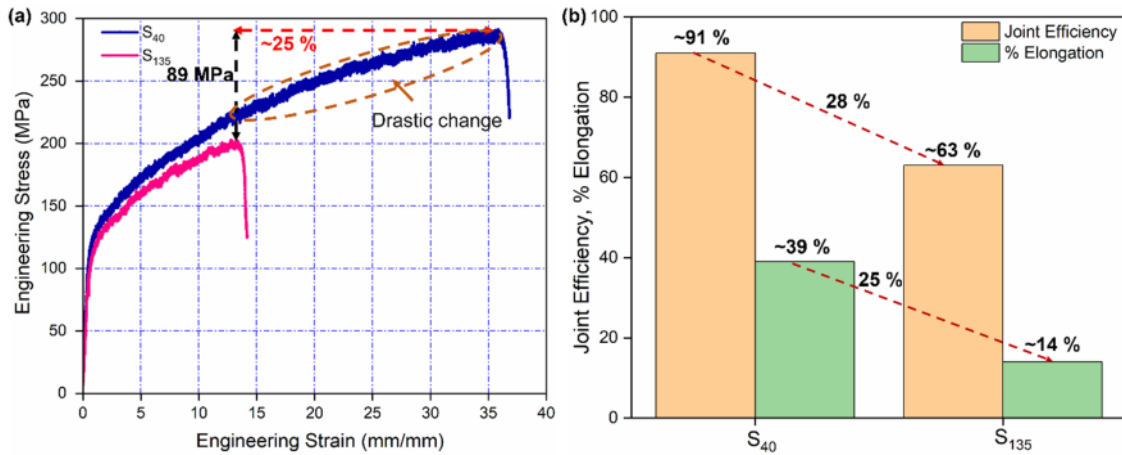


Fig. 5 : (a) Engineering stress-strain curve, and (b) joint efficiency and percentage elongation for different weld conditions (S<sub>40</sub> and S<sub>135</sub>)

Table 4 : Tensile test results obtained for S<sub>40</sub> and S<sub>135</sub> weld conditions

Weld condition	UTS (MPa)	(% EL)	JE (in %)
S40	~292	~39	~91
S135	~203	~14	~63

UTS → ultimate tensile strength, EL → percentage elongation, JE → efficiency of the joint

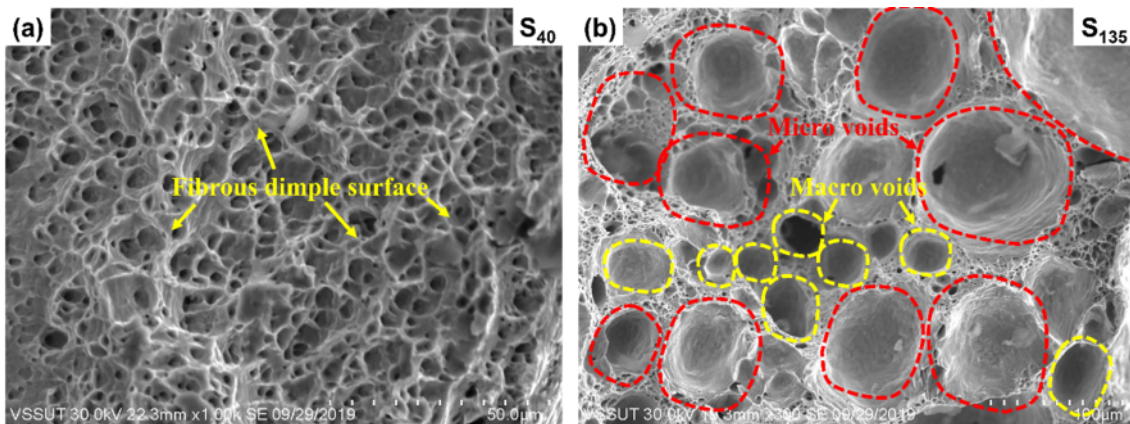


Fig. 6 : Represents fracture surface of the failed tensile specimens for different weld conditions (a) S<sub>40</sub> and (b) S<sub>135</sub>

### 3.4 Electrochemical Testing

To understand the electrochemical behavior of the joints, the  $S_{40}$  and  $S_{135}$  welded specimens are subjected to corrosion testing under 3.5 wt.% NaCl corrosive environment. The graph in **Fig. 7** depicts the Tafel plot for the different weld conditions ( $S_{40}$  and  $S_{135}$ ). The value of  $I_{corr}$  extracted from the Tafel plot is found to increase from  $2.28E-08$  ( $S_{40}$ ) to  $6.61E-05A/cm^2$  ( $S_{135}$ ) with the rise in heat input from 40 to 135 J/mm. As a higher value of  $I_{corr}$  results in a higher corrosion rate [36], the joints prepared under the  $S_{135}$  condition exhibit a higher corrosion

rate (1.273 mm/year). **Table 5** details the value of  $I_{corr}$  and corrosion rate for different weld conditions. Higher heat input (135 J/mm) deteriorates the surface quality with the higher  $R_a$  value ( $\sim 6.13 \mu m$  for  $S_{135}$  for the joints), providing an easy site for attack when exposed to a corrosive environment [34]. Although for different materials, a similar result was reported, and the reason cited was that a higher amount of heat input caused a decrease in corrosion resistance for the joints produced by the GTAW process as compared to the PAW process [37].

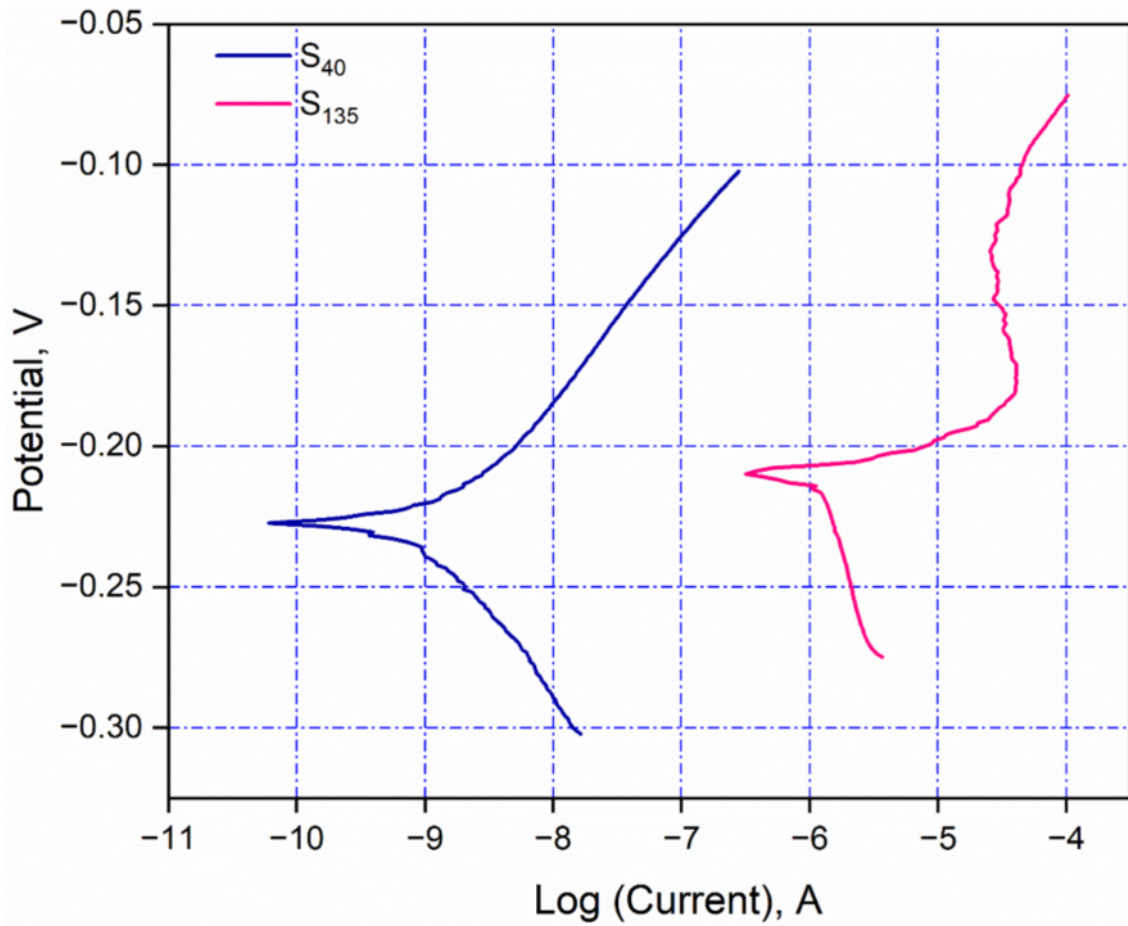


Fig 7 : Illustrates Tafel curve for different weld conditions ( $S_{40}$  and  $S_{135}$ )

Table 5 : Presents electrochemical data obtained for different weld conditions ( $S_{40}$  and  $S_{135}$ )

Weld condition	$I_{corr}$ ( $A.cm^{-2}$ )	Corrosion rate (mm/year)
$S_{40}$	$2.28E-08$	$4.77E-04$
$S_{135}$	$6.61E-05$	1.273

## 4.0 CONCLUSIONS

The present work reports the comparative analysis of the joints fabricated by MPAW and GTAW processes. The acquired results signify the importance of heat input on the joint characteristics. The major outcomes derived from the current experimentation are listed below:

- a) Higher heat input (135 J/mm) deteriorates the surface quality of the joints, which includes a change in the appearance of the bead profile from dark brown to black color and a higher value of surface roughness ( $R_a \sim 0.438 \mu\text{m}$  for  $S_{40}$  and  $R_a \sim 6.13 \mu\text{m}$  for  $S_{135}$ ). Further, a higher value of  $R_a$  ultimately leads to an increase in the corrosion rate of the joints (1.273 mm/year for  $S_{40}$  and 4.77E-04 for  $S_{135}$ ).
- b) Microstructural morphology relies on the value of  $G \times R$ , which is directly governed by the amount of heat supplied for successful joining. Lower heat input (40 J/mm) results in higher  $G \times R$ , which lowers the value of SDAS, leading to finer microstructural features.
- c) A lower amount of heat input (40 J/mm) leads to decreased HAZ and SDAS value, which ultimately enhances the strength and ductility ( $\sim 292 \text{ MPa}$ , 39% for  $S_{40}$  and  $\sim 203 \text{ MPa}$ , 14% for  $S_{135}$ ). Further, the failure mode varies from desirable ductile mode (characterized by numerous dimples for  $S_{40}$ ) to unwanted brittle mode (identified by the presence of micro-and macro-voids for  $S_{135}$ ) as the heat input increases.

The results obtained from the current examination suggest that lower heat input should be utilized to join thin Cu-Ni alloy sheets. The heat input significantly governs the microstructural, mechanical, and electrochemical behavior of the joints. Further, the arc pulsation technique may be utilized in future studies to gain more control over the heat input to achieve additional enhancement in the quality of the joint.

## REFERENCES

- [1] Kou S (2003); *Welding Metallurgy*, N.J. USA, pp. 431-446.
- [2] Dwibedi S, Bag S (2022); Influence of process parameters on microstructural evolution, solidification mode, and impact strength in joining of stainless steel thin sheets, *Adv. Mater. Process. Technol.*, 8, pp. 1089-1104.
- [3] Quigley MBC (1986); *High Power Density Welding*, in *The physics of welding*, Elsevier, pp. 306-329.
- [4] Ireland CLM (1990); *Current State of Power Laser Technology and Future Trends*, *Manuf. Technol.*
- [5] Chaudhary J, Jain NK, Pathak S, Koria SC (2019); Investigations on thin SS sheets joining by pulsed micro-plasma transferred arc process, *Journal of Micro-manufacturing*, 2, pp. 15-24.
- [6] Dwibedi S, Jain NK and Pathak S (2018); Investigations on joining of stainless steel tailored blanks by  $\mu$ -PTA process, *Mater. Manuf. Process.*, 33, pp. 1851-1863.
- [7] Dwibedi S, Bag S, Lodhi DK, Kalita A (2020); Joining of Different Thickness Dissimilar Materials S. SS 316L/SS 310 By  $\mu$ -PAW Process, in *Advances in Additive Manufacturing and Joining*, Springer, pp. 569-578.
- [8] Dwibedi S, Bag S (2021); Development of Micro-plasma Arc Welding System for Different Thickness Dissimilar Austenitic Stainless Steels, *J. Inst. Eng. India Ser. C*, 102, pp. 657-671.
- [9] Kumar P, Sinha AN, Hirwani CK, Murugan M, Saravanan A, Singh AK (2021); Effect of welding current in TIG welding 304L steel on temperature distribution, microstructure and mechanical properties, *J. Braz. Soc. Mech. Sci. Eng.* 43, p. 369.
- [10] Wang X, Hu Q, Li T, Liu W, Tang D, Hu Z, Liu K (2022); Microstructure and Fracture Performance of Wire Arc Additively Manufactured Inconel 625 Alloy by Hot-Wire GTAW, *Metals* 12(3), p. 510.
- [11] Nevcanoğlu A, Bozkurt Y, Salman S (2021); The Effect of TIG Welding Parameters and Automatization for Non-Heat Treated Inconel 718 Sheets, *Arab. J. Sci. Eng.*, 46, pp. 12613-12623.
- [12] Khan FN, Junaid M, Hassan AA, Baig MN (2021); Effect of pulsation in TIG welding on the microstructure, residual stresses, tensile and impact properties of Ti-5Al-2.5Sn alloy, *Proc. Inst. Mech. Eng. Part E J. Process Mech. Eng.*, 235, pp. 361-370.
- [13] Liu Y, Zhang S, Guo C, Long T, Li J (2022); Comparative study on CCTIG welding and PCTIG welding of GH4169 under the same heat input, *Mater. Sci. Technol.*, 38, pp. 1451-1458.
- [14] Kornokar K, Nematzadeh F, Mostaan H, Sadeghian A, Moradi M, Waugh DG, Bodaghi M, (2022); Influence of heat input on microstructure and mechanical properties of gas tungsten arc welded HSLA S500MC steel joints, *Metals*, 12(4), p. 565.
- [15] Baruah M, Bag S (2016); Influence of heat input in microwelding of titanium alloy by micro plasma arc, *Journal of Materials Processing Technology*, 231, pp. 100-112.
- [16] Baruah M, Bag S (2016); Microstructural Influence on Mechanical Properties in Plasma Microwelding of Ti6Al4V Alloy, *J. Mater. Eng. Perform.*, 25, pp. 4718-4728.

- [17] Saikia T, Baruah M, Bag S (2019); On the effect of heat input in plasma microwelding of maraging steel, Proc IMechE, Part B: J Engineering Manufacture, 233, pp. 807-822.
- [18] Saha D, Pal S (2019); Microstructure and Work Hardening Behavior of Micro-plasma Arc Welded AISI 316L Sheet Joint, Journal of Materials Engineering and Performance 28, pp. 2588-2599.
- [19] Haldar V, Biswal SK, Pal S (2022); Formability study of micro-plasma arc-welded AISI 316L stainless steel thin sheet joint, J. Braz. Soc. Mech. Sci. Eng., 44, p. 564.
- [20] Sahu AK, Bag S (2019); Finite Element Modelling and Experimental Verification of Dissimilar Joining Between Inconel 718 and SS 316L by Micro-plasma Arc Welding, in Advances in Computational Methods in Manufacturing, R.G. Narayanan, S.N. Joshi and U.S. Dixit, Eds., Springer Singapore, Singapore, pp. 231-243.
- [21] Sahu AK, Bag S (2020); Effect of Pre-weld Solution Treatment on Mechanical Properties and Microstructure of Micro-Plasma Arc Welded Inconel 718, in Advances in Additive Manufacturing and Joining, M.S. Shunmugam and M. Kanthababu, Eds., Springer Singapore, Singapore, pp. 373-383.
- [22] Orishich AM, Malikov AG, Shelyagin VD, Khaskin VY, Chayka AA (2016); Optimisation of the processes of laser, microplasma and hybrid laser-microplasma welding of aluminium alloys, Weld. Int., 30, pp. 957-961.
- [23] Ferro P, Bonollo F, Tiziani A (2005); Laser welding of copper-nickel alloys: a numerical and experimental analysis, Sci. Technol. Weld. Join., 10, pp. 299-310.
- [24] Devletian JH, Sullivan MJ, Engineer CW (2006); Flux Cored Arc Welding of CuNi 90/10 Piping with CuNi 70/30 Filler Metal, San Diego Portland State Univ. [https://www.nsrp.org/wp-content/uploads/2015/09/Deliverable\\_All\\_Position\\_Flux\\_Cored\\_Electrode\\_Final\\_Report-Portland\\_State\\_University.pdf](https://www.nsrp.org/wp-content/uploads/2015/09/Deliverable_All_Position_Flux_Cored_Electrode_Final_Report-Portland_State_University.pdf)
- [25] Munro C (2013); The Effects of Repeated Weld Repairs on the Mechanical Properties of Copper-Nickel Pipe Joints.
- [26] Chakravarthy M, Ramanaiah N, Sundara Siva Rao B (2014); Effect of laser welding on mechanical properties of 70/30 Cu-Ni alloy welds, Proc. Inst. Mech. Eng. Part B J. Eng. Manuf., 228, pp. 1153-1161.
- [27] Cao X, Nolting A (2019); Autogenous fiber laser welding of 70/30 Cu-Ni alloy plates, Mater. Des., 181, p. 108075.
- [28] Dwibedi S, Bag S (2020); Assessment by destructive and non-destructive approach to characterize 90/10 cupronickel weldments, Mater. Today Proc., 33, pp. 5014-5018.
- [29] Xing S, Bai S, Liu R, Liu Y, Qi J, Hou J, Jhang D (2023); Characterization of Corrosion Behavior and Corrosion Production Property of 90-10 Cupronickel Welding Joints in Flowing Seawater, Metals, 13, p. 294.
- [30] Dwibedi S (2016); Investigation on autogenous joining of stainless steel sheets of different thickness using micro Plasma Transferred Arc ( $\mu$ -PTA) process.
- [31] Maurya AK, Pandey C, Chhibber R (2023); Influence of heat input on weld integrity of weldments of two dissimilar steels, Mater. Manuf. Process., 38, pp. 379-400.
- [32] Torkamany MJ, Hamed MJ, Malek F, Sabbaghzadeh J (2006); The effect of process parameters on keyhole welding with a 400 W Nd: YAG pulsed laser, J. Phys. Appl. Phys., 39, p. 4563.
- [33] Kumar B, Dwibedi S, Bag S (2022); On the interaction of cooling rate with thermal-microstructural-mechanical characteristics of laser-welded  $\alpha+\beta$  titanium alloy, Adv. Mater. Process. Technol., 8, pp. 774-789.
- [34] Abosrra L, Ashour AF, Mitchell SC, Youseffi M (2009); Corrosion of Mild Steel and 316L Austenitic Stainless Steel with Different Surface Roughness in Sodium Chloride Saline Solutions, WIT Press Southampton.
- [35] Nabavi SF, Farshidianfar A, Dalir H (2023); A comprehensive review on recent laser beam welding process: geometrical, metallurgical, and mechanical characteristic modeling, Int. J. Adv. Manuf. Technol., 129, pp. 4781-4828.
- [36] Sahu N, Barik BK, Sahoo S, Badjena SK, Sahoo SK (2021); Studies on metallurgical and corrosion characteristics of dissimilar GTAW welding of alloy 800 and SS316L using multicomponent activated flux, Mater. Today Proc., 44, pp. 2533-2536.
- [37] Chuaiphan W, Kumkoon P, Kalnaowakul P (2023); Dissimilar welding of AISI 201 and 202 low nickel stainless steels by GTA and PA welding processes, J. Alloys Metall. Syst., 4, p. 100047.